NANO · MICRO
small
www.small-journal.com

Etchant-Free Dry-Developable Extreme Ultraviolet Photoresist Materials Utilizing N-Heterocyclic Carbene–Metal Complexes

Dowon Kim, Jinhwan Byeon, Jaeboong Ahn, Sangjin Kim, In-Uk Moon, Huijeong Ryu, Dong Suk Oh, Yang Hun Yoon, Hae-geun Jee, Chan-Cuk Hwang, and Sukwon Hong**

Extreme ultraviolet (EUV) lithography has enabled significant reductions in device dimensions but is often limited by capillary force-driven pattern collapse in conventional wet processes. Recent dry-development approaches, while promising, frequently require toxic etchants or specialized equipment, limiting their broader applicability and highlighting the need for more sustainable, cost-effective alternatives. In this study, highly reactive, etchant-free dry-developable EUV photoresists using N-heterocyclic carbene (NHC)-based metal-ligand complexes, achieving half-saturation at EUV doses of 8.5 or 27 mJ cm^{-2}, are synthesized. A simple thermal dry development process is employed, utilizing a standard furnace to remove unexposed areas of the photoresist, leading to 80 nm resolution with line-edge roughness (LER) comparable to wet-developed patterns. Moreover, EUV-induced chemical reactions of the NHC metal-ligand complexes are investigated via EUV-photoelectron spectroscopy, near-edge X-ray absorption fine structures, X-ray photoelectron spectroscopy, and density functional theory. It is suggested that the high EUV sensitivity of the NHC metal-ligand complexes is attributed to branching polymerization reactions initiated by secondary electron and photoelectron generation. These EUV-sensitive, dry-developable NHC metal–organic photoresists offer a sustainable and economical alternative to conventional techniques, eliminating the need for toxic and corrosive etchants while achieving high-resolution nanopatterns through simple thermal treatment, thus advancing future nanofabrication technologies.

1. Introduction

Advances in semiconductor industries have heightened the demand for cutting-edge lithographic technology. The miniaturization of devices is essential, as dictated by Moore's Law.[1–3] Although deep ultraviolet lithography (DUVL) currently dominates the semiconductor manufacturing market, it demonstrates limited resolution due to the characteristic wavelength (193 nm, E = 6.4 eV) of ArF light sources and diffraction limit as light cannot be focused on a line or spot smaller than half its wavelength. To address the scaling limitations inherent in ArF immersion lithography, extensive efforts were undertaken, enabling the achievement of features near 15 nm through the use of multiple patterning techniques.[4–6] However, this approach resulted in a substantial increase in manufacturing costs and introduced significant yield challenges. These factors, coupled with the physical limitations of further scaling using ArF immersion, ultimately drove the industry to adopt extreme ultraviolet lithography (EUVL) as the preferred technology for continued miniaturization in semiconductor fabrication. EUVL technology uses the short wavelength of an EUV light source (13.5 nm, E = 92 eV). It drastically improves the resolution of the decreasing critical dimensions (CDs) in current nanoscale devices.[7–11]

Despite overcoming the fundamental limitations of DUVL, EUVL presents several significant challenges. The higher energy of EUV photons results in fewer photons at the same dose compared to DUV light, leading to reduced photon flux.[12–14] Additionally, the high energy of EUV photons induces secondary electron-based reaction pathways, which can trigger acid generation and diffusion.[15] As pattern dimensions continue to shrink, conventional chemically amplified resists (CARs) have shown their limitations in achieving high-resolution patterns, often suffering from increased pattern roughness due to the intrinsic properties of their organic polymeric structures.[16] Consequently, producing patterns with ever-decreasing CDs using conventional photoresists has become increasingly challenging,

D. Kim, J. Byeon, J. Ahn, S. Kim, I.-U. Moon, H. Ryu, S. Hong
Department of Chemistry
Gwangju Institute of Science and Technology (GIST)
Gwangju 61005, Republic of Korea
E-mail: shong@gist.ac.kr

D. S. Oh, Y. H. Yoon, H.-geun Jee, C.-C. Hwang
Beamline Research Division
Pohang Accelerator Laboratory (PAL)
Pohang University of Science and Technology (POSTECH)
Pohang 790-784, Republic of Korea
E-mail: cchwang@postech.ac.kr

The ORCID identification number(s) for the author(s) of this article can be found under https://doi.org/10.1002/smll.202407966

DOI: 10.1002/smll.202407966

prompting extensive research into the development of novel EUV PRs specifically engineered for EUVL.

EUV PRs target 10 nm pattern resolution, <20% line edge roughness (LER), and 20 mJ cm^{-2} EUV sensitivity based on the International Roadmap for Devices and Systems.[17] Metal–organic photoresists (MOPRs), specifically metal-oxo cluster–based MOPRs and small molecule-based MOPRs, can achieve high resolution and low LER with a low EUV dose requirement.[18–24] Notably, Sn-oxo cluster-based MOPRs, first reported in 2014, showed promising performance with an 18 nm resolution at a minimum EUV dose of 350 mJ cm^{-2}.[25] Continued progress has led to the achievement of 15 nm patterns with a 20 mJ cm^{-2} EUV dose by 2023.[26] Similarly, small molecule-based MOPRs, especially those utilizing oxalate complexes, have exhibited significant potential, with meticulous screening of metals and ligands enhancing EUV sensitivity, reducing the required dose to 36 mJ cm^{-2}.[27]

To further advance these developments, solvent-free dry processes have been explored to address the limitations of conventional solvent-based wet development methods, such as the risk of pattern collapse due to solvent-induced capillary forces.[28] Industries, such as LAM Research, are at the forefront of developing advanced dry techniques for nanoscale pattern formation.[29,30] However, despite a few attempts to implement these novel dry processes, their application in EUVL to achieve precise nanoscale patterns remains limited, highlighting the need for further innovation in this area.[31–35]

Hwang and co-workers at POSTECH reported pentacene-based EUVL in 2010 through a solvent-free dry development process.[32] This approach leveraged the quasi-polymerization properties of pentacene upon EUV exposure, allowing selective removal of pentacene from unexposed film areas through simple thermal treatment. Ekinci and co-workers later reported a resistless patterning method using HF-treated Si surfaces and tetramethylammonium hydroxide (TMAH) etching, which leveraged the etch resistance of SiO_2.[33] Fairbrother and co-workers demonstrated an all-dry resist technology that employed zinc-imidazolate and 1,1,1,5,5,5-hexafluoroacetylacetone for chemical etching.[34] More recently, Kenane and co-workers at Lam Research developed a dry patterning method for tin-oxo cluster-based resists, using HBr vapor to cleave Sn—O—Sn bonds, leading to pattern development.[35]

Promising advancements in dry deposition processes for resists include molecular layer deposition (MLD) for vertically tailored hybrid multilayers, hafnium-based hybrid thin films, and vapor-phase infiltration for poly(methyl methacrylate) indium oxide (PMMA–InO_x).[36–38] However, despite achieving uniform dry deposition of resists, many of these techniques still rely on wet development processes, highlighting the growing need for widely applicable dry development techniques.

Among these techniques, we focused on thermal dry development, as it eliminates the need for toxic and corrosive etchants during the development process and does not require specialized equipment—a standard furnace is sufficient. However, conventional MOPRs are not well-suited for thermal dry development applications. Metal-oxo cluster-based MOPRs often have high molecular weights, leading to undesirably high sublimation temperatures, while oxalate-based small molecule MOPRs are prone to thermal decomposition. Therefore, designing new highly reactive EUV PRs that can withstand thermal decomposition while maintaining low sublimation temperature and molecular weights is essential.

Organometallic complexes with N-heterocyclic carbene (NHC) ligands can serve as the basis for synthesizing EUV PRs with thermal development capability. NHC ligands are a class of heterocycles featuring carbene and at least one nitrogen atom in a ring structure. NHC ligands are strong σ-electron donors, and the organometallic complexes with NHC ligands often exhibit high stability against heat, moisture, and oxygen. Furthermore, organometallic complexes with NHC ligands can be designed to exhibit low sublimation temperatures. This could be achieved by manipulating bulky functional groups or incorporating halide groups.[39–42] Glessi et al. explored Au(I)–NHC complexes and their sublimation abilities. Complexes with simple side chain structures depicted significantly low sublimation temperatures (<100 °C) at $\approx 10^{-6}$ atm.[42] Organometallic complexes with NHC ligands and diverse metals, including silver (Ag), copper (Cu), and cobalt (Co), have shown similar volatile but stable characteristics. Thus, NHC ligands are promising for developing thermal EUV PRs.[43–45]

Herein, we present a series of EUV PRs [1,3-bis(4-vinylbenzyl)imidazol-2-ylidene–silver chloride ((VinylBn)L-AgCl), 1-isopropyl-3-(4-vinylbenzyl)imidazol-2-ylidene–gold chloride ((*i*-Pr)L-AuCl), and 1-isopropyl-3-(4-vinylbenzyl)imidazol-2-ylidene–gold hexafluorophosphate ((*i*-Pr)L-$AuPF_6$)] using the volatile but stable properties of organometallic NHC complexes. EUV sensitivity was achieved by incorporating Ag, Au, and hexafluorophosphate (PF_6) groups, featuring a high EUV cross-section, and the styrene group further improved the EUV reaction allowing for branching polymerization reactions as summarized in **Figure** 1a. The (VinylBn)L-AgCl and (*i*-Pr)L-$AuPF_6$ showed outstanding EUV sensitivities with values of 9 and 27 mJ cm^{-2} for half-saturated thickness (D_{50}), respectively. Furthermore, using these materials, we achieved 80 nm scale patterns through a thermal dry development method, illustrated in Figure 1b. This study introduces an advanced dry development technique that is both sustainable and economical, eliminating the need for toxic, corrosive etchants, while maintaining high performance through simple thermal treatment with specifically designed materials.[46–49]

2. Results and Discussion

2.1. EUV PRs Based on Organometallic Complexes with NHC Ligands

The EUV PRs were synthesized by using a multi-step strategy to optimize performance as depicted in Scheme S1 (Supporting Information). First, isopropyl groups were incorporated to introduce molecular asymmetry, effectively reducing the sublimation temperature. Second, vinyl groups were introduced to the ligands via an amine substitution reaction, promoting the formation of a polymer network upon EUV exposure. Third, metals, silver and gold, were integrated along with their corresponding ligands (Cl and PF_6) through metalation and ligand exchange reactions. This integration leveraged the EUV sensitivity of the metals for reaction initiation and utilized the robust metal–NHC structure as the backbone, leading to the synthesis of NHC-based small

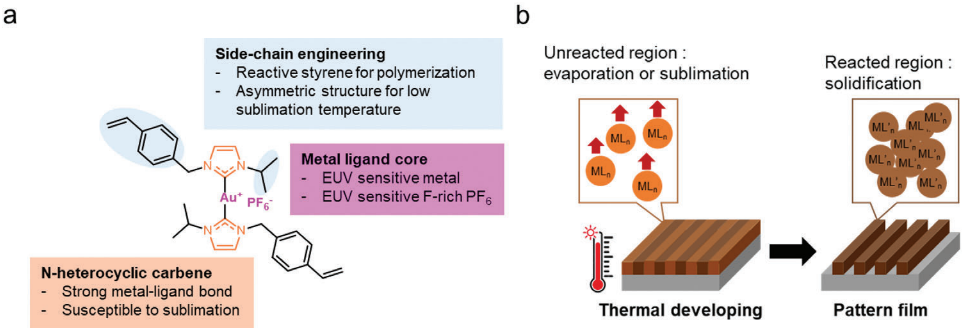

Figure 1. a) Advantages of (*i*-Pr)L-AuPF$_6$ are based on the side chain, metal-ligand core, and N-heterocyclic carbene. b) A schematic diagram of the thermal development method.

molecule metal-organic photoresists (NHC MOPRs) including (VinylBn)L-AgCl, (*i*-Pr)L-AuCl, and (*i*-Pr)L-AuPF$_{6.}$

The structural properties of these complexes were confirmed via single-crystal X-ray diffraction (SC-XRD) as illustrated in **Figure 2a**. (VinylBn)L-AgCl displayed a symmetric dimeric structure with four reactive vinyl groups and two EUV-sensitive silver atoms, promoting network formation and rapid reaction initiation. (*i*-Pr)L-AuCl exhibited an asymmetric structure with two reactive vinyl groups and one EUV-sensitive gold atom, which lowers sublimation temperature and enhances thermal development capability. The (*i*-Pr)L-AuPF$_6$ complex, with its bulky PF$_6^-$ anion, further improves the photoresist by increasing asymmetry, for better thermal development capability, and boosting EUV sensitivity, with its high EUV cross-section.

Thermal stability, a critical factor for thermal development, was assessed using thermogravimetric analysis (TGA) (Figure 2b). All three materials maintained their initial weight at temperatures <300 °C. Subsequent weight loss occurs in the following order: (VinylBn)L-AgCl > (*i*-Pr)L-AuPF$_6$ > (*i*-Pr)L-AuCl. The TGA curves indicate that (VinylBn)L-AgCl, (*i*-Pr)L-AuCl, and (*i*-Pr)L-AuPF$_6$ decomposition is initiated at 340, 292, and 360 °C, respectively. (*i*-Pr)L-AuPF$_6$ depicts the most substantial weight loss (40%), followed by (*i*-Pr)L-AuCl (35%) and (VinylBn)L-AgCl (30%), indicating significant evaporation before thermal decomposition, making it ideal for thermal development. However, the residual weight of the materials at 500 °C after decomposition suggests that thermal development conditions should be optimized to minimize the thermal decomposition of NHC MOPRs.

The sensitivity of NHC MOPRs to EUV exposure was also evaluated. The normalized PR thickness curve was acquired using a microscale mash pattern mask for the EUV dose test. Multiple spots were exposed using an incremental EUV dose for the contrast (γ) curve with the resulting normalized thickness summarized in Figure 2c. (VinylBn)L-AgCl demonstrated the highest EUV sensitivity of 8.5 and 30 mJ cm^{-2} for D_{50} and D_{100}, respectively. Conversely, (*i*-Pr)L-AuCl showed insufficient sensitivity, rendering it impractical for EUV PR applications. However, ligand optimization with (*i*-Pr)L-AuPF$_6$ led to improved EUV sensitivity with values of 27 and 90 mJ cm^{-2} for D_{50} and D_{100}, respectively.

To examine the homogeneity within the resist films, we conducted atomic force microscopy (AFM, Figure S1, Supporting Information), energy-dispersive X-ray spectroscopy (EDS, Figures S2 and S3, Supporting Information), and X-ray diffraction (XRD, Figure S4, Supporting Information). AFM analysis confirmed uniform spin-coated films with low surface roughness. XRD revealed the amorphous structure of the resist films, while EDS verified well-distributed atomic composition within the films. These findings collectively confirm the structural uniformity and homogeneity of the resist film.

The high reactivity of (VinylBn)L-AgCl and (*i*-Pr)L-AuPF$_6$ was investigated through EUV-based photoelectron spectroscopy (PES) (**Figure 3a,b**). The spectra reveal photoelectrons with a kinetic energy of ≈80 eV, originating from the 4d and 5d valence orbitals of Ag and Au, respectively.[50,51] The photoelectrons generate excess secondary electrons with low energy (<80 eV) through their inelastic scattering with atoms (Figure 3c).[52–54] Chemical reactions, including the attachment, ionization, or excitation of molecules initiated by low-energy electrons, are the reaction pathways of compounds during EUV irradiation.[55] Therefore, generating a large number of low-energy secondary electrons causes the high reactivity of (VinylBn)L-AgCl and (*i*-Pr)L-AuPF$_6$.

2.2. Extreme Ultraviolet Lithography

Based on the high EUV sensitivity of NHC MOPR, the lithography ability of the as-prepared compounds was investigated through line/space pattern formation. A 92 eV synchrotron EUV light source was passed through a transmission diffraction mask fabricated via ArF lithography. We used a transmission mask made with ArF lithography on a 100 nm silicon nitride (Si_3N_4) membrane with tantalum absorber patterns (**Figure 4**). Linear grating masks with a 100 to 80 nm half-pitch were used in these experiments and this was placed near the targeted wafer to form the desired pattern utilizing EUV interference lithography.[33] The process mechanism is illustrated in Figure 4a.

The top-view scanning electron microscopy (SEM) and atomic force microscopy (AFM) results demonstrate the EUV-exposed image and properties of patterns (Figure 4b,c). The Si_3N_4 membrane absorbs ≈60% of the EUV light, while residual tantalum in the open areas of the mask further reduces EUV transmission (Figure S5, Supporting Information), requiring a higher EUV dose.[56] Additionally, limitations in the nanoscale control of the exposure system made it challenging to accurately quantify the contrast in the energy absorbed by the patterned regions of the resist layer. Despite these challenges, the desired pattern was successfully achieved with a dose of ≈4 J cm^{-2} illuminated onto

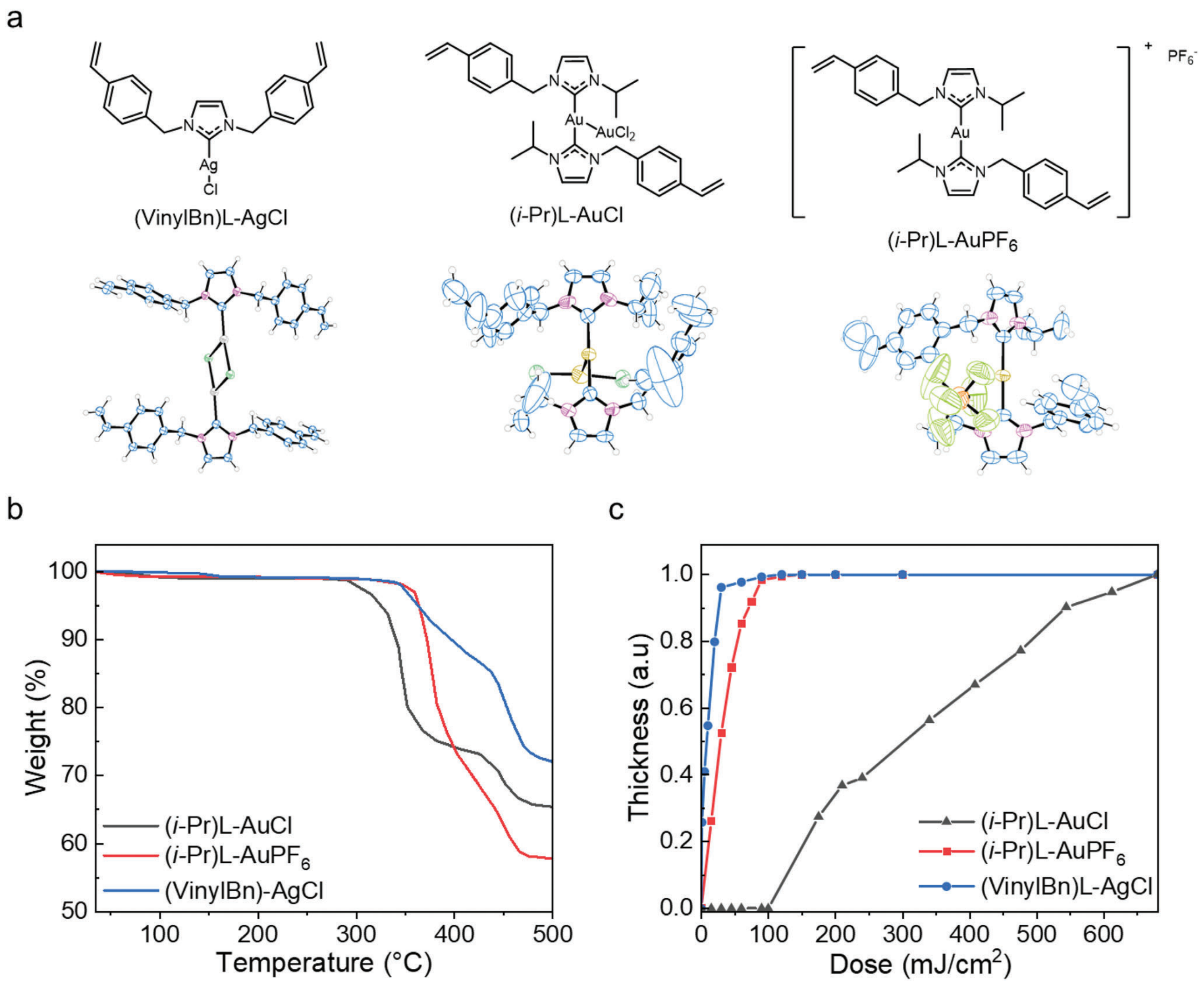

Figure 2. a) Chemical and crystal structures of NHC MOPRs. b) Thermogravimetric analysis and c) dose-thickness contrast (γ) curve of NHC MORPs. For the crystal structures, thermal ellipsoids are set at 50% probability. The hydrogen atoms are omitted for clarity. The selected bond lengths (Å) and angles (°) of (VinylBn)L-AgCl: Ag(1)—Cl(1) = 2.3845(6) Å, Ag(1)—C(1) = 2.091(2) Å, C(1)—N(1) = 1.361(3) Å, C(1)—N(2) = 1.348(4) Å, Ag(1)—Cl(1)—Ag(1′) = 89.35(2)°, and N(1)—C(1)—N(2) = 103.7(2)°, (*i*-Pr)L-AuCl: Au(1)—C(1) = 2.03(1) Å, Au(1)—Au(2) = 3.006(2) Å, Au(2)—Cl(1) = 2.317(5) Å, Au(2)—Cl(2) = 2.318(6) Å, C(1)—N(1) = 1.35(2) Å, C(1)—N(2) = 1.32(2) Å, Au(1)—Au(2)—Cl(1) = 96.9(1)°, Au(1)—Au(2)—Cl(2) = 98.2(2)°, C(1)—Au(1)—Au(2) = 94.3(4)°, and N(1)—C(1)—N(2) = 106(1)°, and (*i*-Pr)L-AuPF$_6$: Au(1)—C(1) = 2.021(3) Å, Au(1)—C(2) = 2.016(3) Å, C(1)—N(1) = 1.355(6) Å, C(1)—N(2) = 1.340(6) Å, P(1)—F(1) = 1.558(6), P(1)—F(2) = 1.541(6), C(1)—Au(1)—C(2) = 178.7(2)°, N(1)—C(1)—N(2) = 106.0(4)°, and F(1)—P(1)—F(2) = 89.3(4)°.

the mask from above for both (VinylBn)L-AgCl and (*i*-Pr)L-AuPF$_6$ films. An extended exposure beyond this dose could induce overreaction and reduce line-space contrast, leading to lower pattern resolution.

Thus, the nanoscale patterns were acquired through EUV interference lithography as illustrated in Figure 4b, which highlights the SEM and AFM image of 80 nm CD (VinylBn)L-AgCl lines developed in THF after 30 s exposure at ≈4 J cm^{-2} dose. The AFM pattern reveals ≈13 nm LER, 9 nm average height, and a relatively flat space area. The SEM image depicts a grainy texture of (VinylBn)L-AgCl patterns, which elevates the LER of the pattern and suppresses the small resolution pattern formation. The SEM image (Figure 4c) of 80 nm CD (*i*-Pr)L-AuPF$_6$ indicates a smooth pattern with 9 nm LER and 10 nm depth, as confirmed by AFM analysis. A significant degree of the observed LER was influenced by the inherent roughness of the ArF-prepared masks, given the high LER value of the masks, as shown in Figure S5 (Supporting Information).[57,58]

We analyzed the thermal development capability of NHC MORPs under EUV light. TGA results (Figure 2b) highlight the need to lower the sublimation temperature of NHC MORPs to prevent ligand decomposition, achievable under reduced pressure. We used a vacuum pump to acquire the reduced pressure of 10^{-4} atm for condition screening.

Initial screening of pristine NHC MORP films at various temperatures demonstrated that (*i*-Pr)L-AuPF$_6$ films achieved optimal development at 110 °C. Above 120 °C, however, deformation occurred, leading to incomplete material removal. In contrast,

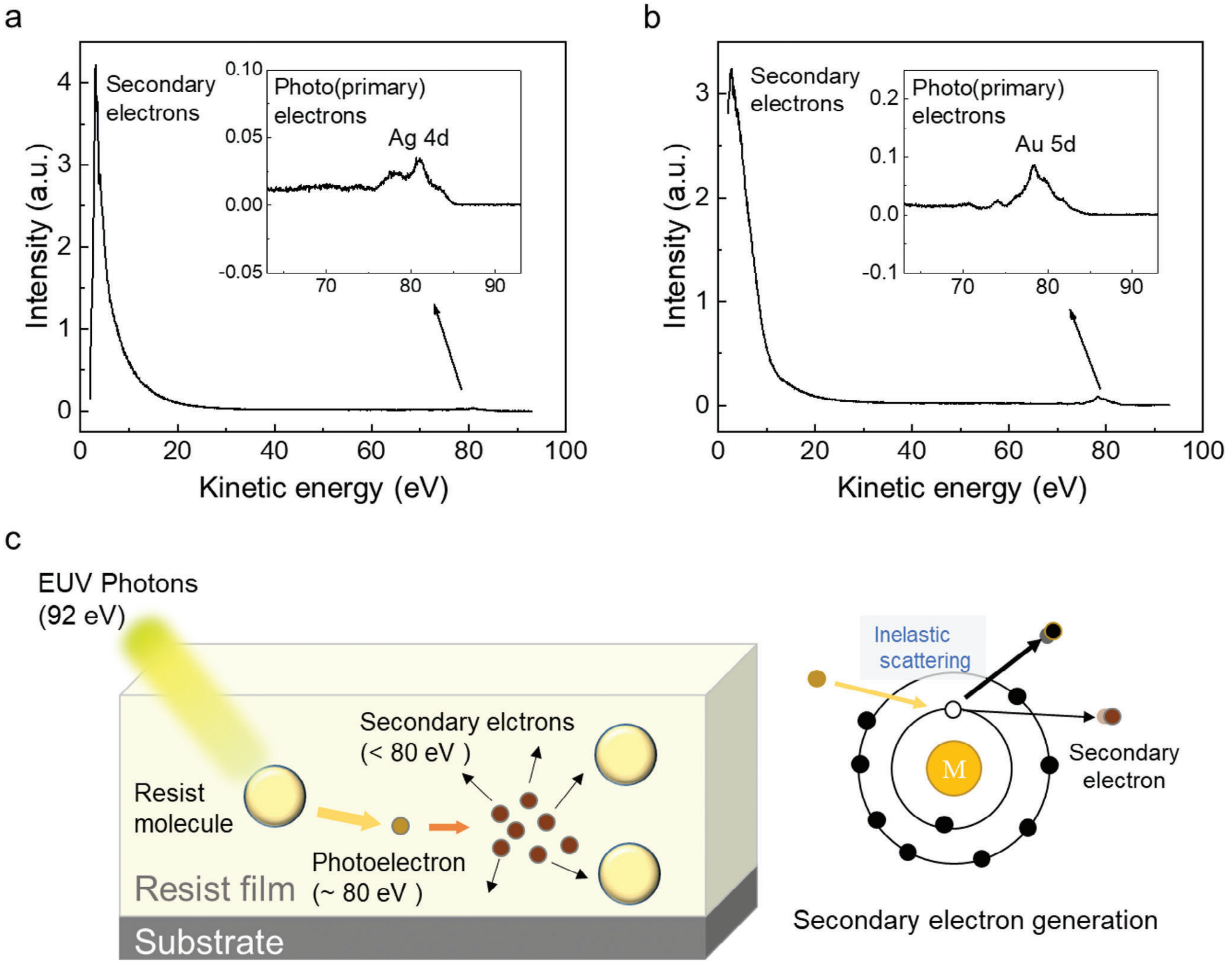

Figure 3. EUV-based PES results of a) (VinylBn)L-AgCl and b) (*i*-Pr)L-AuPF¬6 with EUV irradiation ranging from 5 to 100 eV. c) Schematic diagram illustrating the generation of photoelectrons and secondary electrons induced by an EUV photon.

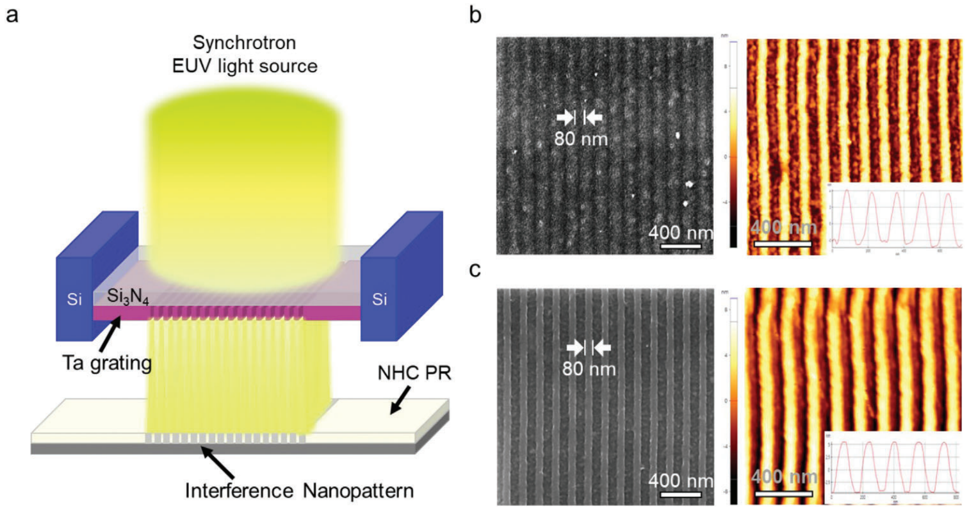

Figure 4. a) Schematic of synchrotron EUV source Talbot pattern lithography. Top-view SEM and AFM images of b) 80 nm CD (VinylBn)L-AgCl patterns and c) 80 nm CD (*i*-Pr)L-AuPF$_6$ patterns.

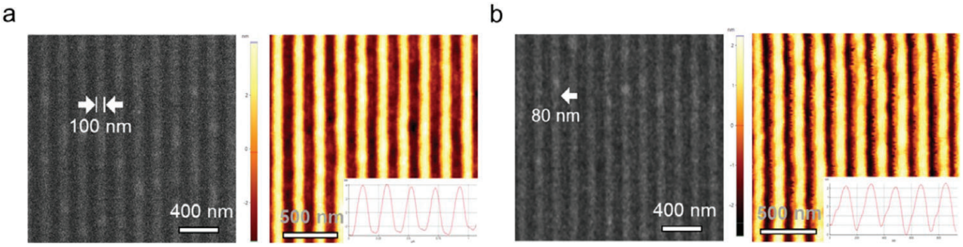

Figure 5. Top-view SEM and AFM images of thermally developed a) 100 nm and b) 80 nm (*i*-Pr)L-AuPF$_6$ line patterns. The AFM image insets show the average height profile of NHC PR lines.

(VinylBn)L-AgCl films began to deform at v100 °C, prior to sublimation, resulting in thicker films remaining post-development, as depicted in Figure S6 and Table S1 (Supporting Information). This behavior can be attributed to the weaker NHC—Ag bond strength compared to the NHC—Au bond, resulting in lower stability and faster decomposition of (VinylBn)L-AgCl.[59] Consequently, (*i*-Pr)L-AuPF$_6$ was selected as the candidate for dry photoresist.

Optimized film coating parameters for line-space contrast and LER were established using DUV-exposed patterns for the initial screening as shown in Figure S7 and Table S2 (Supporting Information). The accessibility of DUV-exposed patterns facilitated this process, with commercially available 1 µm masks used for pattern generation. By adjusting the spin-coating speed, we controlled the film thickness from 45 nm at 3000 rpm to 28 nm at 5000 rpm. Further optimization of development time identified optimal conditions at 5000 rpm (28 nm thickness) and 110 °C for 30 min, yielding high-contrast patterns with LER performance comparable to traditional wet development methods. Preliminary tests suggest that development time may be shortened under higher vacuum (6×10^{-9} atm) conditions (Figure S8, Supporting Information).

The thermally developed patterns under dry conditions with extended air exposure before development often exhibited lower quality. This issue was effectively mitigated by briefly exposing the patterns to THF vapor, which improved pattern quality not by altering the chemical structure but by controlling the hydrogen bonds between PF_6^- and water molecules, enabling faster removal. This is supported by the XPS analysis of the film illustrated in Figure S9 (Supporting Information), which shows no significant difference after air exposure and THF treatment. During air exposure, (*i*-Pr)L-AuPF$_6$ film absorbs water, which interferes with the sublimation process by forming hydrogen bonds with the PF_6^- anion.[60] After the vapor-phase insertion of THF, the hydrogen bonding between the PF_6^- anion and water competes with the hydrogen bonding between THF and water.[61] As a result, the proportion of PF_6^- anions participating in hydrogen bonding with water decreases, promoting effective sublimation.

The optimized conditions of 10^{-4} atm pressure, 110 °C temperature, and 30 min evaporation time enabled the production of high-contrast patterns comparable to those obtained through wet processes. (**Figure 5**) By utilizing the EUV interference lithography method and optimized development conditions, patterns with CDs of 100 and 80 nm were successfully generated, as depicted in Figure 5a and b, respectively. AFM analysis revealed that the average height of the dry-developed patterns was 7 nm, with a line edge roughness (LER) of 7 nm for the 100 nm CD pattern, and 6 nm with an LER of 10 nm for the 80 nm CD pattern. Both patterns demonstrated LER that was comparable to or improved upon, those of wet-developed patterns. Notably, this outcome was achieved without the use of toxic solvents or etchants, utilizing only a highly accessible furnace and vacuum pump. This demonstrates the potential of etchant-free thermal dry development methods.

2.3. EUV-Induced Chemical Reaction Analysis

To get a further understanding of chemical reactions upon EUV exposure in NHC MORPs as a function of EUV dose, near-edge X-ray absorption fine structure (NEXAFS) analysis was performed with the 10D HRPES beamline in the Pohang Accelerator Laboratory (PAL) (**Figure 6**a,b). We focused on the C and F K-edge spectra region to determine the covalent bond peaks of the as-prepared compounds. To minimize photochemical reactions during the NEXAFS measurements, the scan range was restricted to 282–292 eV, with the effect of the scan range on the carbon peaks shown in Figure S10 (Supporting Information). The reaction saturation was investigated with the incremental EUV doses of (VinylBn)L-AgCl (5, 15, and 30 mJ cm^{-2}) and (*i*-Pr)L-AuPF$_6$ (30, 60, and 90 mJ cm^{-2}). Figure 6a reveals the spectra of (VinylBn)L-AgCl with a decrease in peak intensity from 286–288 eV, with the most significant decrease at 287 eV. Figure 6b shows that the changes in the spectra of (*i*-Pr)L-AuPF$_6$ are similar to those of (VinylBn)L-AgCl, suggesting that (*i*-Pr)L-AuPF$_6$ and (VinylBn)L-AgCl follow similar reaction pathways.

To determine the origin of this change, we performed a comparative analysis of the covalent bond peak positions associated with vinyl benzyl groups and NHC ligands, potential reaction sites, incorporating data from previous peak analysis reports (Figure S11, Supporting Information).[62–64] By comparing 1,3-Bis(2,4,6-trimethylphenyl)imidazol-2-ylidene-silver chloride (IMes-AgCl), which contains double bonds in the NHC backbone, with 1,3-Bis(2,4,6-trimethylphenyl)-4,5-dihydroimidazol-2-ylidene-silver chloride (SIMes-AgCl), which lacks these double bonds, we identified the peaks corresponding to double bonds in NHC groups at ≈287 eV, as shown in Figure S3a (Supporting Information). Our analysis suggests that the double bond character in the NHC ligand contributes to the polymerization process.

A moderate decrease in peak intensity near the 286 eV in Figure 6a,b implies a reaction on the vinyl group of the styrene. A comparative study between (VinylBn)L-AgCl, which contains

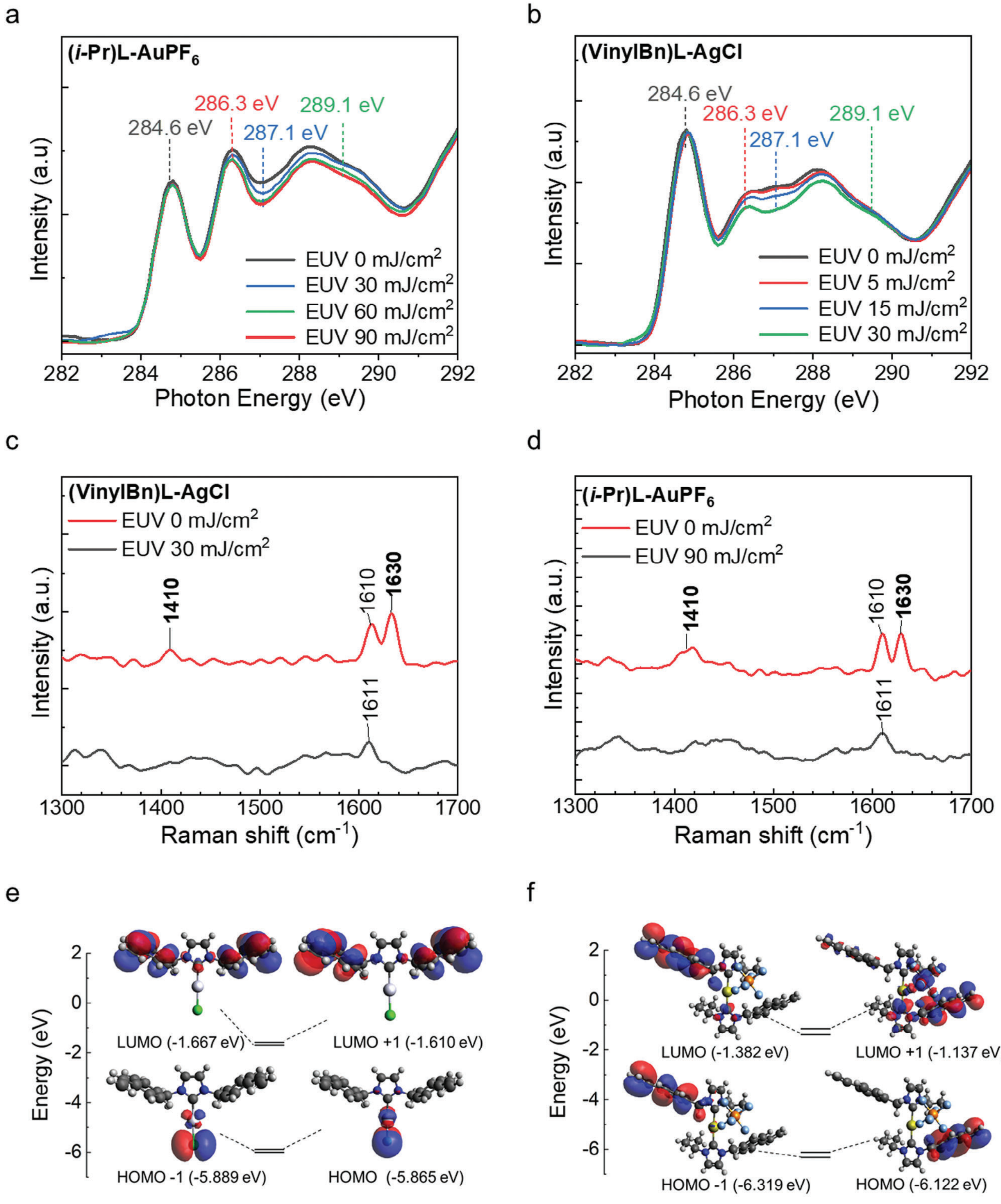

Figure 6. Fitted NEXAFS spectra of the C K-edge region of a) (VinylBn)L-AgCl before and after 5, 15, and 30 mJ cm^{-2} EUV exposure, and b) (*i*-Pr)L-AuPF$_6$ before and after 30, 60, and 90 mJ cm^{-2} EUV exposure. The Raman spectra of c) (VinylBn)L-AgCl and d) (*i*-Pr)L-AuPF$_6$. The calculated HOMOs and LUMOs of e) (VinylBn)L-AgCl and f) (*i*-Pr)L-AuPF$_6$ through DFT.

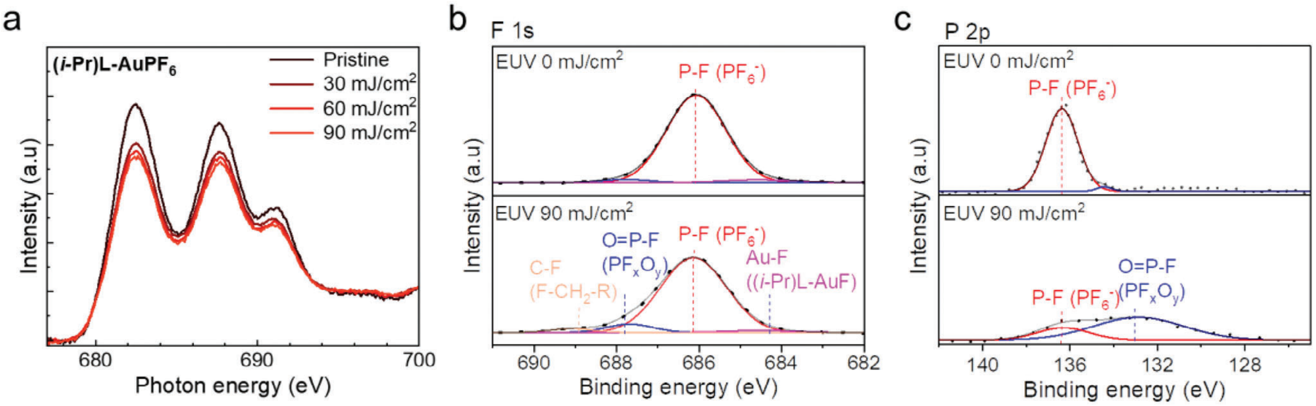

Figure 7. a) NEXAFS spectra of the F K-edge region of (*i*-Pr)L-AuPF$_6$ with incremental EUV doses. The comparison of the XPS spectra of (*i*-Pr)L-AuPF$_6$ b) F 1s and c) P 2p regions before and after EUV exposure.

vinyl groups, and 1,3-bis(4-ethylbenzyl)imidazol-2-ylidene–silver chloride ((EthylBn)L-AgCl) complexes, which lacks them, showed a similar moderate decrease in intensity near the 286 eV region (Figure S11b, Supporting Information). This shift is indicative of the modification of the double bond in the vinyl groups to a single bond. These results suggest that an EUV-induced vinyl benzyl polymerization reaction is present.

To further confirm the presence of vinyl group reactions, Raman spectroscopy can effectively examine chemical reactions, particularly those involving C═C double bonds in ligands. Figure 6c,d shows the Raman spectra of unreacted (VinylBn)L-AgCl and (*i*-Pr)L-AuPF$_6$ (EUV 0 mJ cm^{-2}) with the main bands present at 1410, 1600, and 1647 cm^{-1}, each corresponding to Vinyl $\delta(=\mathrm{CH_2})$, Ring $\nu(\mathrm{C=C})$, and Vinyl $\nu(\mathrm{C=C})$, as reported in previous studies.[65] The bands corresponding to the vinyl groups (1412 and 1630 cm^{-1}) disappear while the band at 1610 cm^{-1} remains after EUV exposure for both (VinylBn)L-AgCl (EUV 30 mJ cm^{-2}) and (*i*-Pr)L-AuPF$_6$ (EUV 90 mJ cm^{-2}) showing a peak shift often observed in styrene polymerization. This result provides evidence of EUV-induced vinyl benzene polymerization.

Considering that both NHC double bond and vinyl group can act as acceptors to secondary electrons, we hypothesized that the secondary electrons are likely to be populated into the lowest unoccupied molecular orbital (LUMO) of the molecules.[66] The LUMO and highest occupied molecular orbital (HOMO) of each compound were obtained through density functional theory (DFT) calculations to identify the destination of secondary electrons. The LUMOs of (VinylBn)L-AgCl and (*i*-Pr)L-AuPF$_6$ appear on the styrene moiety of the compounds with energies of −1.667 and −1.382 eV, respectively. This suggests the insertion of secondary electrons into the vinyl groups which can lead to polymerization reaction of NHC MOPRs.

Fluorine radical generation has been reported to play a significant role in crosslinking inorganic resists by enhancing or altering the reactivity of functional groups within the resist matrix.[67–69] This contributes to photo-induced processes, such as radical generation, which modify the structural and chemical integrity of the resist during lithography. The high EUV cross-section of PF$_6^-$ further prompted an analysis of its contribution to the polymerization process. PF$_6^-$ alterations were analyzed through F K-edge NEXAFS, as depicted in **Figure** 7a. The spectra reveal distinct peaks at 682.5, 687.7, and 691.3 eV, corresponding to the presence of PF$_6^-$.[70] The intensity of the peaks declined after EUV-irradiation, with the most significant changes observed at 682.1 eV, followed by the peaks at 687.7 and 691.3 eV, highlighting the dissociation of the P—F bond in PF$_6^-$. NEXAFS analysis confirms that P—F bond cleavage occurs upon EUV exposure, suggesting that the cleaved F atoms are likely involved in the polymerization process.

To further explore the implication of P—F bond dissociation, the (*i*-Pr)L-AuPF$_6$ film was further analyzed using XPS before and after EUV exposure (Figure 7b,c). The results reveal a trend consistent with PF$_6^-$ decomposition reaction pathways, including the generation of F radicals.[71,72] The F 1s spectrum analysis in Figure 7b reveals that the P—F (686.5 eV) peak from PF$_6^-$ is dominant before EUV exposure, with traces of the O═P—F (687.8 eV) peak present from the oxidized PF$_x$O$_y$. However, upon EUV exposure, the intensity of the O═P—F peak increases, and a new C—F peak (689 eV) emerges. The increase in the O═P—F peak and the generation of the new C—F peak is more clearly shown in Figure S12 (Supporting Information), where we subtracted the unreacted (EUV 0 mJ/cm^2) F 1s X-ray photoelectron spectroscopy (XPS) from the EUV-reacted (EUV 90 mJ/cm^2) F 1s XPS in Figure 7b after normalizing the two graphs.

The generation of the C—F bond peak, as revealed by XPS analysis, and the decomposition of PF$_6^-$, evidenced by NEXAFS analysis, suggest the formation of F radicals. These radicals likely initiate polymerization by reacting with vinyl groups to form C—F bonds. The location of the C—F XPS peak provides evidence that a single F atom is bonded to vinyl benzyl groups, shifting the peak to higher energy compared to that of the F atom in the PF$_6^-$ anion (Figure 7b). Furthermore, the presence of remaining PF$_x$ is indicated by the formation of PF$_x$O$_y$ during air exposure and the thermal development process. We observed a significant increase in the O═P—F peak in the F 1s spectrum (Figure 7b) and the O—P (132.5 eV) peak in the P 2p spectrum (Figure 7c) after EUV exposure, suggesting the formation of PF$_x$O$_y$ from remaining PF$_x$. In addition, the presence of the Au—F peak indicates that some decomposed F atoms bind to gold metal, forming a metal-halide bond, though it does not influence the polymerization reaction and results in a ligand exchange reaction.

Building upon these analyses, we propose two potential reaction pathways depicted in **Figure 8** comprising radical polymerization initiated by F radical from PF_6^- and the anionic polymerization of (*i*-Pr)L-AuPF_6 styrene. NEXAFS and XPS analyses reveal the decomposition of PF_6^- with the P—F bond dissociation and C—F bond formation during EUV exposure. Based on these results, the proposed EUV-induced radical polymerization reaction mechanism of (*i*-Pr)L-AuPF_6 is depicted in Figure 8a. The generated secondary electrons induce cation generation on the (*i*-Pr)L-AuPF_6 film for charge neutralization (Figure 3b). Secondary electron emission from PF_6^- dissociates the P—F bond to generate F radicals. This initiates radical polymerization, which is indicated by the formation of new C—F species after EUV exposure.[73–75]

DFT calculations, NEXAFS measurements at the C K-edge, and Raman spectroscopy studies indicate that the secondary electrons target the LUMO of the styrene moiety in NHC ligands, followed by anion polymerization. The styrene groups, upon gaining an extra electron, form styryl radical anions, which subsequently dimerize to produce distyryl dianion, as previously reported.[76,77] These dianionic species initiate anionic propagation to build a polymeric structure. The reactivity of the adjacent NHC double bonds is evident through NEXAFS peak analysis, indicating that the adjacent NHC double bonds are involved in polymerization. Thus, electron-initiated (*i*-Pr)L-AuPF_6 reaction pathways are proposed (Figure 8b). The polymerization pathways at multiple reaction sites form intricate branched polymer structures (Figure 8c). This facilitates rigid pattern formation and enhances pattern contrast by improving the sublimation temperature of polymers.

3. Conclusion

In this study, we developed NHC MOPRs ((VinylBn)L-AgCl, (*i*-Pr)L-AuCl, and (*i*-Pr)L-AuPF_6) using wet and dry methods and demonstrated their nanopatterning capabilities. These materials demonstrated remarkable EUV sensitivity, with (VinylBn)L-AgCl requiring 8.5 mJ cm^{-2} and (*i*-Pr)L-AuPF_6 needing 27 mJ cm^{-2} EUV doses for D_{50}. These properties played a pivotal role in achieving high-resolution nanopatterning. An 80 nm wide, dense pattern was produced with a transmission mask-based synchrotron EUVL source. The significant difference in sublimation temperature between EUV-reacted and unreacted materials, combined with the robustness of intricate polymer structures, enabled successful thermal development. This approach produced 80 nm dry-developed patterns with quality comparable to wet-developed patterns, underscoring the potential of this simple, non-toxic thermal treatment method.

Additionally, through NEXAFS, Raman, and XPS analysis, we proposed two possible EUV-induced chemical reaction pathways of the NHC MOPRs: i) radical polymerization of the styrene moiety initiated by F radical produced through P—F bond decomposition during secondary electron generation and ii) anion polymerization of the styrene moiety and NHC double bond initiated by secondary electron attachment to the LUMO of the styrene moiety. These insights demonstrate that NHC MOPRs, with their promising thermal development capabilities, offer a significant breakthrough for future EUV photoresists, providing a sustainable and economic alternative to conventional lithographic techniques by eliminating the need for toxic and corrosive etchants, enabling high-resolution patterning through straightforward thermal processes, and advancing high-resolution dry lithography technologies, thereby paving the way for more efficient and environmentally friendly nanofabrication practices.

4. Experimental Section

Materials: n-Hexane (GR grade), acetone, tetrahydrofuran (THF), methylene chloride (CH_2Cl_2), acetonitrile, ethyl ether (GR grade), and ethanol (HPLC grade) were procured from DUKSAN Reagents. All the chemicals were bought from Sigma–Aldrich Co, ThermoFisher Scientic Inc., and Sejin CI Co. The chemicals were utilized without further purification.

1-(4-Vinylbenzyl)-1H-Imidazole: Sodium bicarbonate ($NaHCO_3$) (2.63 g, 31.4 mmol) and imidazole (6.8 g, 50 mmol) were dissolved in a 50-mL binary mixture of water and acetone (1:1 mixture). 4-Vinylbenzyl chloride (3.39 mL, 24 mmol) was added dropwise to the mixture after stirring at room temperature. The solution was heated at 50 °C and stirred for 22 h at this temperature. The solution was filtered to remove the unreacted salt while concentrating the filtrate under reduced pressure. The product was dissolved in ethyl ether and washed thrice with 50 mL of deionized water. The organic phase was washed thrice using 2.0 M hydrochloric acid (HCl) and washed with 4.0 M sodium hydroxide (NaOH). The final product was extracted using ethyl ether and dried using anhydrous magnesium sulfate ($MgSO_4$). The solution was concentrated under reduced pressure to obtain the final product. Clear liquid (52%); 1H NMR (400 MHz, CDCl3) (δ ppm) = 5.101(s, 2H), 5.263(dd, J = 0.8, 11.4 Hz, 1H), 5.755(dd, J = 0.8, 18.3 Hz, 1H), 6.685(dd, J = 10.7, 17.6 Hz, 1H), 6.899(t, J = 1.1 Hz, 1H), 7.086–7.122 (m, 3H), 7.385(d, 2H), 7.544(s, 1H)

1,3-Bis(4-Vinylbenzyl)-1H-Imidazolium Chloride: 4-Vinylbenzylchloride (7.45 mL, 50 mmol) and 1-(4-vinylbenzyl)-1H-imidazole (6.8 g, 50 mmol) were dissolved in 50-mL acetonitrile. The mixture was stirred for 24 h at 70 °C. The solution was concentrated under reduced pressure and washed using 40-mL THF to retrieve a yellowish solid product (78%); 1H NMR (400 MHz, CDCl3) (δ ppm) = 5.264 (d, 2H, J = 10.9 Jz), 5.520 (s, 4H), 5.755(dd, J = 17.9 Hz, 2H), 6.635(dd, J = 10.7, 17.6 Hz, 2H), 7.22–7.23(m, 2H), 7.32–7.43 (m, 8H), 11.08(s, 1H).

(VinylBn)L–AgCl: 1,3-Bis(4-vinylbenzyl)-1H-imidazolium chloride (1.65 g, 5 mmol) was dissolved in 15-mL CH_2Cl_2. Ag_2O (0.75 g, 3 mmol) was added, stirring the solution for 24 h. The solution was filtered through the celite. The filtrate was concentrated under reduced pressure. n-Hexane was introduced to the concentrated filtrate. A white solid product was obtained as a residue, which was dried using a vacuum. White solid (86%); 1H NMR (400 MHz, CDCl3) (δ ppm) = 5.264 (s, 4H), 5.27 (d, J = 13.2 Jz, overlapping 2H), 5.755 (d, J = 17.6 Hz, 2H), 6.695 (dd, J = 10.7, 17.6 Hz, 2H), 6.912 (s, 2H), 7.21(d, J = 8.2 Hz, 4H), 7.40 (d, J = 8.2 Hz, 4H)

1-Isopropyl-3-(4-Vinylbenzyl)-1H-Imidazolium Chloride: 4-Vinylbenzylchloride (7.45 mL, 50 mmol) and 1-isoproyl-1H-imidazole (5.5 g, 50 mmol) were dissolved in 50-mL acetonitrile and stirred for 24 h at 70 °C. The solution was concentrated under reduced pressure and was washed using 40 mL THF to obtain a solid product. Yellow solid (78%); 1H NMR (400 MHz, DMSO) (δ ppm) = 1.473 (d, 6H, J = 6.9 Jz), 4.636 (m, 1H), 5.305 (d, 1H, J = 10.30), 5.390 (s, 2H), 5.875 (d, J = 17.6 Hz, 1H), 6.735(dd, J = 10.7, 17.6 Hz, 1H), 7.410(dd, 4H), 7.882 (dd, 2H), 9.437 (s, 1H)

(i-Pr)L–AuCl: 1-Isopropyl-3-(4-vinylbenzyl)-1H-imidazolium chloride (1.31 g, 5 mmol) was dissolved in 15-mL CH_2Cl_2. Ag_2O (0.75 g, 3 mmol) was added to the solution, stirred for 24 h, and filtered using celite. Chloro(dimethyl sulfide)Au(I) [(SMe_2)AuCl] (1.47 g, 5 mmol) was added to the solution, stirred for 24 h at room temperature, and filtered using celite to obtain a clear solution. The filtrate was concentrated under reduced

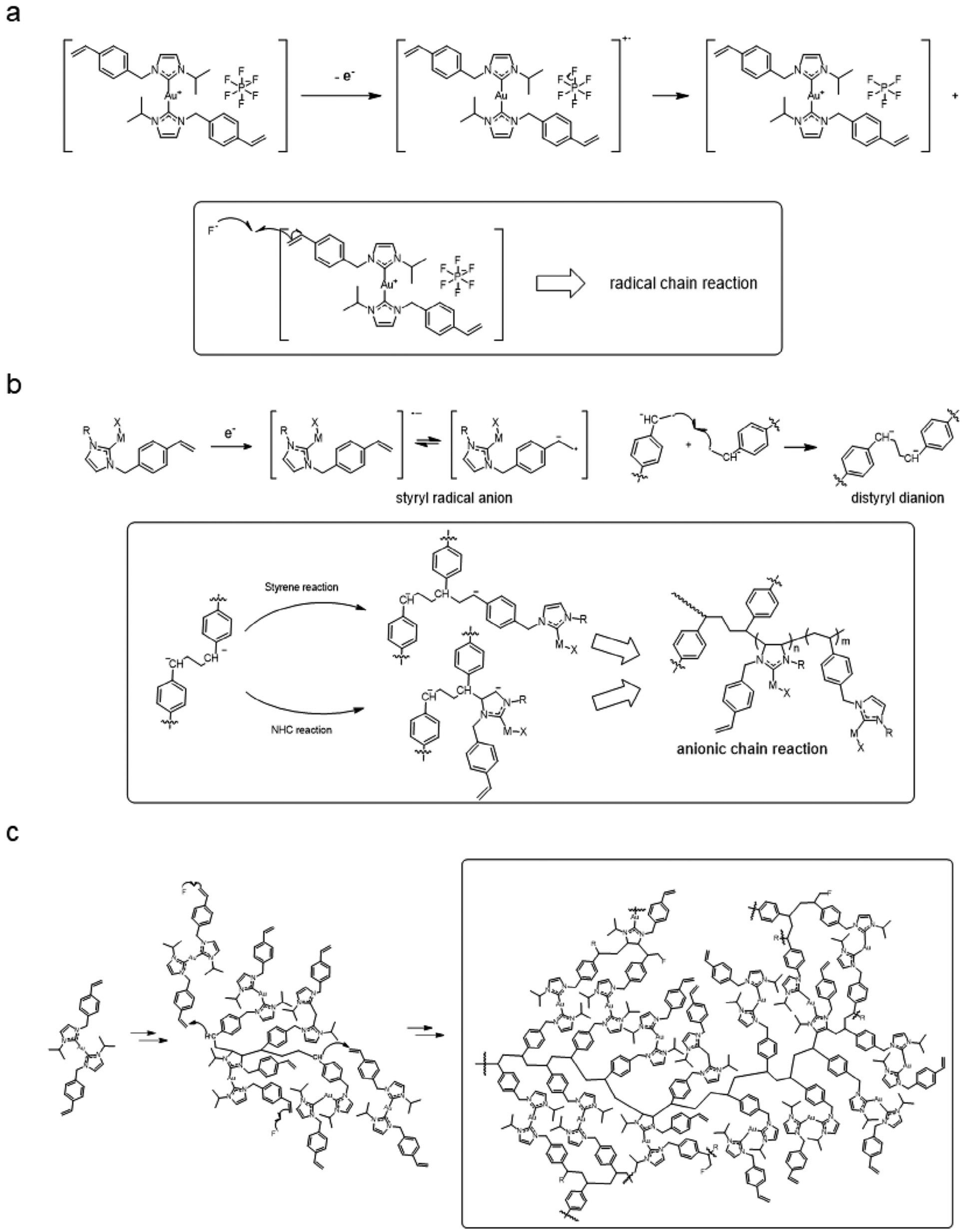

Figure 8. a) Hole-initiation reaction by the (i-Pr)L-AuPF$_6$ cation radical. b) The electron-initiation reaction of NHC PR anion radicals induced by EUV photons. c) The branching polymerization of (i-Pr)L-AuPF$_6$ through crosslinking reactions.

pressure. n-Hexane was added to the concentrated solution. A white solid product was precipitated and dried under a vacuum. White solid (56%); 1H NMR (400 MHz, CDCl3) (δ ppm) = 1.47 (d, 6H), 5.08 (m, 1H), 5.27 (d, 1H, J = 10.3), 5.33 (s, 2H), 5.75 (d, 1H), 6.70 (dd, 1H), 6.90 (m, 2H), 7.28 (m, 2H), 7.39 (m, 2H)

(i-Pr)L–AuPF$_6$: A solution of (*i*-Pr)L–AuCl(397 mg, 0.5 mmol) was prepared in 15 mL MeOH. NH_4PF_6 (120 mg, 0.75 mmol) was added to the solution and stirred for 48 h. The solution was concentrated under reduced pressure. The product was dissolved in CH_2Cl_2 and filtered using celite. The filtrate was concentrated under reduced pressure. Adding n-hexane to the concentrated filtrate precipitated a white solid product, which was dried under a vacuum. White solid (60%); 1H NMR (400 MHz, CDCl3) (δ ppm) = 1.50 (d, 6H, J = 6.9 Jz), 4.77 (m, 1H), 5.26 (d, 1H, J = 10.3), 5.27 (s, 2H, overlapped), 5.72 (d, J = 17.6 Hz, 1H), 6.661 (dd, J = 10.7, 17.6 Hz, 1H), 7.064 (m, 2H), 7.140 (m, 2H), 7.340(m, 2H). 19F NMR (400 MHz, CDCl3) δ(ppm) = −72.29, −74.17

Material Characterization: The thermal properties of PR materials were analyzed with a thermogravimetric analyzer (TGA-50, Shimadzu). TGA was performed at 15–400 °C at a heating rate of 10 °C min^{-1} under an N2 atmosphere. Near computational calculations were conducted at the B3LYP/6-31G(d) level. The unreported compounds were validated through NMR (JEOL; 400 MHz for 1H NMR and 75.4 MHz for 13C NMR). NEXAFS and EUV lithography were performed at the 10D beamlines of the PAL in Korea. The atomic interaction of Ag, Au, C, N, O, and P atoms was analyzed through XPS (K-ALPHA+). The Raman spectrum (NRS-5100) analysis was performed using a 532-nm laser. AFM was performed with an XE-100 atomic force microscope (Park Systems, Inc.) and a PPP-NCHR 10 ᴍ cantilever. Field emission scanning electron microscopy (FE-SEM) was performed using a JSM-7500F+EDS field emission scanning electron microscope (Oxford).

Film Fabrication: The Si films were cleaned using deionized water, acetone, and isopropyl alcohol for 15 min each using a sonicator. PR solutions were prepared by dissolving 10 mg of each material within their respective solvents. (VinylBn)L-AgCl and (*i*-Pr)L-AuCl were dissolved in a 1:1 solution of CH_2Cl_2:THF while (*i*-Pr)L-AuPF$_6$ was dissolved in THF. The samples used for lithography were prepared by spin coating the solutions of each PR at 3000 rpm for 30 s with (VinylBn)L-AgCl and 5000 rpm for 30 s with (*i*-Pr)L-AuPF$_6$. The coated films were used without further treatment.

Lithography Procedure: DUV exposure experiments used an AC-3 ultraviolet (UV) ozone cleaner (AhTech LTS) as the light source. The dosage of the light was determined using a light sensitizer. EUV lithography was performed at the 10D beamlines of the PAL in Korea. Desired pattern masks were kept directly above each coated film. The samples were loaded inside a high vacuum chamber and exposed to the EUV light source. The mask utilized for lithography was prepared using Si3N4. A tantalum-based mask was prepared using an XT1250D ArF dry scanner (ASML) at the National Nanofab Center. The wet development process of (VinylBn)L-AgCl and (*i*-Pr)L-AuCl was conducted with a CH_2Cl_2:THF::1:1 mixture, while THF was used for (*i*-Pr)L-AuPF$_6$. The EUV-exposed films were dipped into their respective developer for 30 s for pattern development.

Thermal Development Process: A thermal furnace linked with a vacuum pump helped in thermal development. A boat was placed in the vacuum furnace and heated to 130 °C before an EUV-reacted film was placed in it for 30 min. The EUV-reacted film was exposed to THF vapor and positioned adjacent to a sealed vial with THF. Then, the film was placed in the boat and inside a vacuum furnace set at 130 °C for 30 min for pattern development.

Supporting Information

Supporting Information is available from the Wiley Online Library or from the author.

Acknowledgements

D.K., J.B., and J.A. contributed equally to this work. This research was supported by the Nano-Material Technology Development Program through the National Research Foundation of Korea (NRF) funded by the Ministry of Science and ICT (NRF-2021M3H4A1A02055667, NRF-2021M3H4A1A02055684, RS-2023-00234622). Research reported in this paper was performed at PLS-II of PAL, which is supported by the Ministry of Science and ICT (MIST) and Pohang University of Science and Technology (POSTECH). The authors acknowledge the National NanoFab Center (NNFC) for providing fabrication facilities.We acknowledge the National NanoFab Center (NNFC) for providing fabrication facilities. We also thank GiSung Lee at the National NanoFab Center (NNFC) for fabricating the interference mask used in this study

Conflict of Interest

The authors declare no conflict of interest.

Data Availablity Statement

The data that support the findings of this study are available from thecorresponding author upon reasonable request.

Keywords

dry development technique, extreme ultraviolet, metal–organic photoresists, N-heterocyclic carbene, near-edge X-ray absorption fine structure

Received: September 4, 2024
Revised: November 21, 2024
Published online: January 23, 2025

[1] X. Lin, M. Qiu, F. Wang, L. He, J. J. C. Lou, in *Handbook of Integrated Circuit Industry*, (Eds.: Y. Wang, M. H. Chi, J. J. C. Lou), Springer Nature Singapore, Germany **2024**, pp. 165–186.
[2] B. Wu, A. Kumar, *Appl. Phys. Rev.* **2014**, *1*, 011104.
[3] C. M. Melliar-Smith, D. E. Haggan, W. W. Troutman, *Bell Labs Tech. J.* **2002**, *2*, 15.
[4] J. H. Chen, L. J. Chen, T. Y. Fang, T. C. Fu, L. H. Shiu, Y. T. Huang, N. Chen, D. C. Oweyang, M. C. Wu, S. C. Wang, J. C. Lin, C. K. Chen, W. M. Chen, T. S. Gau, B. J. Lin, R. Moerman, W. Gehoel-van Ansem, E. van der Heijden, F. de Jong, D. Oorschot, H. Boom, M. Hoogendorp, C. Wagner, B. Koek, *Proc. SPIE* **2005**, *5754*, 13.
[5] O. Soichi, N. Hiroyuki, *Proc. SPIE* **2003**, *5040*, 724.
[6] P. Xu, Y. Chen, Y. Chen, L. Miao, S. Sun, S. W. Kim, A. Berger, D. Mao, C. Bencher, R. Hung, C. Ngai, *Proc.SPIE* **2011**, *7973*, 79731Q.
[7] L. Li, X. Liu, S. Pal, S Wang, C. K. Ober, E. P. Giannelis, *Chem. Soc. Rev.* **2017**, *46*, 4855.
[8] A. Pirati, R. Peeters, D. Smith, S. Lok, A. W. E. Minnaert, M. van Noordenburg, J. Mallmann, N. Harned, J. Stoeldraijer, C. Wagner, C. Zoldesi, E. van Setten, J. Finders, K. de Peuter, C. de Ruijter, M. Popadic, R. Huang, M. Lin, F. Chuang, R. van Es, M. Beckers, D. Brandt, N. Farrar, A. Schafgans, D. Brown, H. Boom, H. Meiling, R. Kook, *Proc. SPIE* **2015**, *9422*, 94221P.
[9] A. Lio, *Synchrotron Radiation News* **2019**, *32*, 9.
[10] M. Thiyagarajan, K. Dean, K. E. Consalves, *J. Photopolym. Sci. Technol.* **2005**, *18*, 737.
[11] J. W. Thackeray, V. J. Jain, S. Coley, M. Christianson, D. Arriola, P. LaBeaume, S. J. Kang, M. Wagner, J. W. Sung, J. Cameron, *J. Photopolym. Sci. Technol.* **2011**, *24*, 179.
[12] P. D. De Bisschop, E. Hendrickx, *Proc. SPIE* **2019**, *957*, 109570.
[13] L. S. Melvin, U. Welling, Y. Kandel, Z. A. Levinson, H. Taoka, H. J. Stock, W. Demmerle, *Jpn. J. Appl. Phys.* **2022**, *61*, SD1030.

[14] K. Sah, A. Cross, M. Plihal, V. Anantha, R. Babulnath, P. De Bisschop, S. Halder, D. Fung, *Proc. SPIE* **2018**, *10809*, 1080909.
[15] J. Torok, R. D. Re, H. Herbol, S. Das, I. Bocharova, A. Paolucci, L. E. Ocola, C. Ventrice Jr, E. Lifshin, G. Denbeaux, L. R. Brainard, *J. Photopolym. Sci. Technol.* **2013**, *26*, 625.
[16] T. Kozawa, J. J. Satillan, T. Itani, *Jpn. J. Appl. Phys.* **2013**, *52*, 076502.
[17] O. Yildirim, E. Buitrago, R. Hoefnagels, M. Meeuwissen, S. Wuister, G. Rispens, A. van Oostem, P. Derks, J. Finders, M. Vockenhuber, Y. Ekinci, *SPIE* **2017**, *143*, 10143.
[18] S. Tarutani, H. Tsubaki, T. Fujimori, H. Takizawa, T. Goto, *J. Photopolym. Sci. Technol.* **2014**, *27*, 645.
[19] B. Cardineau, R. Del Re, M. Marnell, H. Al-Mashat, M. Vockenhuber, Y. Ekinci, C. Sarma, D. A. Freedman, R. L. Brainard, *Microelectron. Eng.* **2014**, *127*, 44.
[20] H. Xu, V. Kosma, E. Giannelis, C. K. Ober, K. Sakai, *Proc. SPIE* **2018**, *10583*, 1058306.
[21] J. Stowers, D. A. Keszler, *Microelectron. Eng.* **2009**, *86*, 730.
[22] T. Minoru, S. Yuta, K. Reiji, Y. Yoshiyuki, T. Koichi, I. Toshiro, *In Proc.* **2016**, *9779*, 97790G.
[23] W. D. Hinsberg, S. A. Meyers, *Proc. SPIE* **2017**, *10146*, 1014604.
[24] J. Passarelli, M. Murphy, R. D. Re, M. Sortland, J. Hotalen, L. Dousharm, R. Fallica, Y. Ekinci, M. Neisser, D. A. Freedman, R. L. Brainard, *J. Micro Nanolithogr. MEMS MOEMS* **2015**, *14*, 043503.
[25] B. Cardineau, R. Del Re, M. Marnell, H. Al-Mashat, M. Vockenhuber, Y. Ekinci, C. Sarma, D. A. Freedman, R. L. Brainard, *Microelectron. Eng.* **2014**, *127*, 44.
[26] J. R. Wu, T. A. Lin, Y. R. Wu, P. H. Chen, T. S. Gau, B. J. Lin, P. W. Chiu, R. S. Liu, *Nanoscale Adv.* **2023**, *5*, 3033.
[27] M. Wilklow-Marnell, D. Moglia, B. Steimle, *J. Micro Nanolithogr. MEMS MOEMS* **2018**, *17*, 1.
[28] K. Yoshimoto, C. Higgins, A. Raghunathan, J. G. Hartley, D. L. Goldfarb, H. Kato, K. Petrillo, M. E. Colburn, J. Schefske, O. Wood, T. I. Wallow, *Proc. SPIE* **2011**, *7972*, 7972.
[29] B. Volosskiy, T. W. Weidman, S. S. Tan, C. Wu, K. Gu, (Lam Research Corporation) *U.S. Patent US20220020584A1*, **2022**.
[30] T. W. Weidman, K. L. Nardi, D. Dictus, B. Kam, C. Wu, E. C. Hansen, N. Kenane, K. L. Gu, (Lam Research Corporation) *U.S. Patent US20220299877A1*, **2022**.
[31] P. Corkery, K. E. Waltz, P. M. Eckhert, M. Ahmad, A. Kraetz, Y. Miao, D. T. Lee, M. K. Abdel-Rahman, Y. Lan, P. Haghi-Ashtiani, A. Stein, J. A. Boscoboinik, M. Tsapatsis, D. H. Fairbrother, *Adv. Funct. Mater.* **2024**, *34*, 2311149.
[32] H. G. Jee, H. N. Hwang, J. H. Han, J. Lim, H. J. Shin, Y. D. Kim, H. H. Solak, C. C. Hwang, *ACS Nano* **2010**, *4*, 4997.
[33] L. T. Tseng, P. Karadan, D. Kazazis, P. C. Constantinou, T. J. Z. Stock, N. J. Curson, S. R. Schofield, M. Muntwiler, G. Aeppli, Y. Ekinci, *Sci. Adv.* **2023**, *9*, eadf5997.
[34] S. A. MacDonald, H. Schlosser, H. Ito, N. J. Clecak, C. G. Willson, *Chem. Mater.* **1991**, *3*, 435.
[35] N. Kenane, A. D. Silva, A. Haider, L. Hoang, C. C. Huang, B. Kam, J. Y. Kim, Y. Lee, D. Li, S. Tan, *J. Photopolym. Sci. Technol.* **2024**, *37*, 257.
[36] S. Yasmeen, S. W. Ryu, S.-H. Lee, H.-B.-R. Lee, *Adv. Mater. Technol.* **2023**, *8*, 2200876.
[37] J. Shi, A. Ravi, N. E. Richey, H. Gong, S. F. Bent, *ACS Appl. Mater. Interfaces* **2022**, *14*, 27140.
[38] A. Subramanian, N. Tiwale, W.-I. Lee, K. Kisslinger, M. Lu, A. Stein, J. Kim, C.-Y. Nam, *Adv, Mater, Interface* **2023**, *10*, 2300420.
[39] I. Selvakumar, N. Boysen, M. Bürger, A. Devi, *Chemistry* **2023**, *5*, 2038.
[40] K. J. Blakeney, P. D. Martin, C. H. Winter, *Organometallics* **2020**, *39*, 1006.
[41] H. J. Arachchilage, L. Suescun, C. L. Ward, C. H. Winter, *Polyhedron* **2021**, *197*, 115010.
[42] C. Glessi, A. Mahgoub, C. W. Hagen, M. Tilset, *Beilstein J. Nanotechnol.* **2021**, *12*, 257.
[43] N. Boysen, A. Philip, D. Rogalla, M. Karppinen, A. Devi, *Chemistry* **2022**, *28*, e202103798.
[44] K. Lubitz, V. Sharma, S. Shukla, J. H. J. Berthel, H. Schneider, C. Hoßbach, *Organometallics* **2018**, *37*, 1181.
[45] N. Boysen, T. Hasselmann, S. Karle, D. Rogalla, D. Theirich, M. Winter, T. Riedl, A. Devi, *Angew. Chem. Int. Ed. Engl.* **2018**, *57*, 16224.
[46] S. S. Tan, J. Yu, D. Li, Y. FAN, Y. Pan, J. Marks, R. A. Gottscho, D. Peter, T. W. Weidman, B. Volosskiy, W. Yang, United States US US20220244645A1, **2022**.
[47] P. A. F. Herbert, J. Braddell, S. MacKenzie, R. G. Woodham, J. R. Cleaver, *Microelectron. Eng.* **1994**, *23*, 263.
[48] S. J. Pearton, R. J. Shul, F. Ren, *MIJ-NSR* **2000**, *5*, e11.
[49] K. Arshak, M. Mihov, D. Sutton, A. Arshak, S. B. Newcomb, *Microelectron. Eng.* **2003**, *67*, 130.
[50] M. G. Mason, *Phys. Rev. B* **1975**, *11*, 5094.
[51] G. M. Bancroft, T. Chan, R. J. Puddephatt, J. S. Tse, *Inorg. Chem.* **1982**, *21*, 2946.
[52] I. Bespalow, Y. Zhang, J. Haitjema, R. M. Tromp, S. J. Molen, A. M. Brouwer, J. Jobst, S. Castellanos, *ACS Appl. Mater. Interfaces* **2020**, *12*, 9881.
[53] O. Kostko, B. Xu, M. Ahmed, D. S. Slaughter, D. F. Ogletree, K. D. Closser, D. G. Prendergast, P. Naulleau, D. L. Olynick, P. D. Ahby, Y. Liu, W. D. Hinsberg, G. M. Wallraff, *J. Chem. Phys.* **2018**, *149*, 154305.
[54] R. Fallica, S. J. Rezvani, S. Nannarone, S. Borisov, D. D. Simone, S. Babin, G. Lorusso, G. Vandenberghe, *Proc. SPIE* **2019**, *10960*, 1096009.
[55] G. Lim, K. Lee, S. Choi, H. J. Yoon, *Coord. Chem. Rev.* **2023**, *493*, 215307.
[56] E. E. Gallagher, J. Vanpaemel, I. Pollentier, H. Zahedmanesh, C. Adelmann, C. Huyghebaert, R. Jonckheere, J. U. Lee, *Proc. SPIE* **2015**, *9635*, 96350X.
[57] P. P. Naulleau, G. M. Gallatin, *Appl. Opt.* **2003**, *42*, 3390.
[58] C. A. Mack, *Proc. SPIE* **2009**, *7488*, 748828.
[59] C. Boehme, G. Frenking, *Organometallics* **1998**, *17*, 5801.
[60] S. A. Katsyuba, M. V. Vener, E. E. Zvereva, Z. Fei, R. Scropelliti, G. Laurenczy, N. Yan, E. Paunescu, P. J. Dyson, *J. Phys. Chem. B* **2013**, *117*, 9094.
[61] P. K. Sahu, A. Chaudhari, S.-L. Lee, *Chem. Phys. Lett.* **2004**, *368*, 351.
[62] K. G. Latham, M. I. Simone, W. M. Dose, J. A. Allen, S. W. Donne, *Carbon* **2017**, *114*, 566.
[63] C. Kolczewski, R. Püttner, M. Martins, A. S. Schlachter, G. Snell, M. M. Sant'Anna, K. Hermann, G. Kaindl, *J. Chem. Phys.* **2006**, *124*, 034302.
[64] J. Sedlmair, S. C. Gleber, C. Peth, K. Mann, J. Niemeyer, J. Thieme, *J. Soils Sediments* **2012**, *12*, 24.
[65] Y. Joseph, M. Wühn, A. Niklewski, W. Ranke, W. Weiss, C. Wöll, R. Schlögl, *Phys. Chem. Chem. Phys.* **2000**, *2*, 5314.
[66] L. K. Noda, O. A. Sala, *Spectrochim. Acta A Mol. Biomol. Spectrosc.* **2000**, *56A*, 145.
[67] L. Wu, I. Benspalow, K. Witte, O. Lugier, J. Haitjema, M. Vockenhuber, Y. Ekinci, B. Watts, A. M. Brouwer, S. Castellanos, *J. Mater. Chem. C* **2020**, *8*, 14757.
[68] Y. K. Kang, H. Kim, S. J. Lee, D.-S. Oh, Y.-H. Yoon, C.-J. Kim, G. Y. Yeom, C.-C. Hwang, M.-G. Kim, *Appl. Surf. Sci.* **2024**, *656*, 159564.
[69] Y. K. Kang, S. J. Lee, S. Eom, B. G. Kim, C.-C. Hwang, M.-G. Kim, *J. Mater. Chem. C* **2024**, *12*, 15855.
[70] K. Medjanik, A. Chernenkaya, X. Kozina, S. Nepijko, G. Ohrwall, P. Foury-Leylekian, P. Alemany, G. Schönhense, E. Canadell, *E. J. Phys. Chem. A* **2016**, *2PF6*, 120.

[71] H. Zhou, T. Li, W. Liu, Z. Guo, Z. Su, J. Gao, M. Qu, G. A. Peng, *ChemSusChem* **2023**, *16*, 202300186.
[72] Y. Li, F. Lian, L. Ma, C. Liu, L. Yang, X. Sun, K. Chou, *Electrochim. Acta* **2015**, *168*, 261.
[73] D. Mroz, J. Hartwig, S. Neitzel-Grieshammer, *ECS Adv.* **2023**, *2*, 030506.
[74] D. Zhou, Y. B. He, Q. Cai, X. Qin, B. Li, H. Du, Q. H. Yang, F. Kang, *J. Mater. Chem. A* **2014**, *2*, 20059.
[75] A. M. Haregewoin, A. S. Wotango, B. J. Hwang, *Energy Environ. Sci.* **2016**, *9*, 1955.
[76] M. Szwarc, **1956**, *178*, 1168.
[77] A. Hirao, S. Loykulnant, T. Ishizone, *Prog. Polym. Sci.* **2002**, *27*, 1399.